

KINEMATIC CHARACTERISTICS OF ICEBERG D28 DRIFT USING SATELLITE DATA SENTINEL-1A/B SAR

A. E. Pogrebnoi¹  and V. N. Belokopytov^{*,1} ¹Marine Hydrophysical Institute RAS, Sevastopol, Russia* **Correspondence to:** Vladimir Belokopytov, belokopytov.vn@mhi-ras.ru

Abstract: The goal of the article is to track down the giant tabular iceberg D28 trajectory from its calving in September 2019 from Amery Ice Shelf until reaching the western part of the Weddell Sea in March 2023 and to present characteristics of the iceberg state and movement, derived from satellite radar data. The Maximally Stable Extremal Regions (MSER) method, which used as an imagery recognition technique for time-dependent visual conditions, has been applied to automatically identify iceberg's positions. On the basis of the Sentinel-1A/B SAR data during 1,275 days, time-series of D28 location, spatial orientation, mass, area, moment of inertia, linear and angular velocity, kinetic and rotational energy, grounding location are presented. D28 dynamics display strongly pronounced regionality, generalized into the three distinct sections of its drift along the Antarctic coast. These sections are in good agreement with existent concepts in the oceanographic literature, concerning the system of Antarctic Slope Current / Antarctic Slope Front.

Keywords: Antarctic, iceberg D28, iceberg dynamics, satellite radar imaging, iceberg grounding, Antarctic Slope Current.

Citation: Pogrebnoi, A. E., V. N. Belokopytov (2024), Kinematic Characteristics of Iceberg D28 Drift Using Satellite Data Sentinel-1A/B SAR, *Russian Journal of Earth Sciences*, 24, ES6005, EDN: JDLXMM, <https://doi.org/10.2205/2024es000940>

1. Introduction

The development of remote sensing methods has provided new, comprehensive opportunities for monitoring the polar regions of the World Ocean, which were impossible in the recent past. Accompanied by field measurements, it enables to detect dozens of large iceberg calvings and trace their further motion [Budge and Long, 2018; Morozov et al., 2021; Stuart and Long, 2011]. From a practical point of view, tracking icebergs is a traditional task of maritime safety and offshore oil and gas production. In the environmental aspect, icebergs plough up bottom sediments during grounding events, cause underwater landslides, and affects vital activity of marine benthos [Barnes and Souster, 2011; Normandeau et al., 2021]. Climatic importance of the icebergs formation process is evident, since it accounts for a significant part of the total mass loss of Antarctic glaciers [Liu et al., 2015]. In addition to the direct loss of glacier mass, iceberg calvings lead to a change of grounded ice flow dynamics from the interior regions of Antarctic to the ocean, increasing its speed [Greenbaum et al., 2015; Hogg and Gudmundsson, 2017; Smith et al., 2019]. The fundamental question: is whether the frequency and intensity of iceberg calving a stationary process that maintains the long-term stable state of the glacier and weakly depends on external forcing [King et al., 2009; Li et al., 2020] or it directly responds to global warming signal [Pritchard et al., 2012; Shepherd et al., 2018] is still understood incompletely.

One of the such events was calving the gigantic tabular iceberg D28, which broke off in September 2019 from the Amery Ice Shelf (AIS) in East Antarctic. According to [Fricker et al., 2002], the cycle of icebergs calving in AIS is 60–70 years and the last major event occurred in 1963–1964. Several works have been devoted to the physical conditions preceding the birth of D28 and the external disturbances that led to the final iceberg detachment from the glacier [Francis et al., 2021; Walker et al., 2021; Zhu et al., 2021]. The drift path and D28 characteristics, such as speed, moving direction, rotation, size, area,

RESEARCH ARTICLE

Received: 13 March 2024

Accepted: 11 October 2024

Published: 30 December 2024



Copyright: © 2024. The Authors. This article is an open access article distributed under the terms and conditions of the Creative Commons Attribution (CC BY) license (<https://creativecommons.org/licenses/by/4.0/>).

draft, grounding locations, calculated from SCATSAT and Sentinel data for the period from September 2019 to February 2021, were considered in [Liu *et al.*, 2021; Mitkari *et al.*, 2021; Singh *et al.*, 2021, 2023].

The purpose of this article is to track down the iceberg D28 path from its calving in the Commonwealth Sea in September 2019 until reaching the western part of the Weddell Sea in March 2023 and to present the characteristics of the motion and state of the iceberg, supplementing them, in comparison with previous works, by new parameters.

2. Materials and Methods

2.1. Iceberg Selection

To select objects in satellite snapshots automatically, various image analysis methods are used, including those developed for computer vision technologies. The Canny Edge Detection method is sufficiently widespread [Canny, 1986; McIlhagga, 2010], according to which the boundaries of an object are determined by the maximum brightness gradient of the image, previously smoothed with the Gaussian filter. It was used to search the boundaries of glaciers and icebergs, for example, in [Mitkari *et al.*, 2021; Singh *et al.*, 2021, 2023; Yu *et al.*, 2019]. Another widely used method is the Constant False Alarm Rate (CFAR) [Gandhi and Kassam, 1988], based on the digital filters related to the local region statistics. To study ice shelves and icebergs CFAR was used in [Silva and Bigg, 2005; Zhu *et al.*, 2021]. Histogram method determines the threshold value to minimize internal variance of the black and white pixels distribution [Otsu, 1979]. It was applied to identify surface manifestations of internal waves and ice floes in the Arctic Ocean [Pogrebnoi, 2023]. Also, methods designed to classify continental landscapes are used to select icebergs, such as the Object Based Image Analyzes (OBIA) [Mazur *et al.*, 2017], machine learning methods [Barbat *et al.*, 2021] and many others.

In this work the Maximally Stable Extremal Regions (MSER) method was applied to identify iceberg D28, which is commonly used for visual pattern recognition, while processing a stream of images under changing conditions of observations, such as different perspectives, lighting, complicated rotations and object deformations [Matas *et al.*, 2004]. For icebergs, which are also rotating and deformed objects, the application of this method seems to be promising.

In case when the iceberg touched the ice shelf or neighboring ice floes and its visible shape was significantly distorted, it was necessary to use manual image processing and at the same time keeping strict control over the selection subjectivity. High albedo of the snow surface usually enables clearly identify icebergs as objects with high brightness. During the Antarctic summer (January–February) or when entering temperate latitudes, the iceberg images become darker as the snow melts. These difficulties can be partly solved by the image inversion. The main problem in object detection arises when the brightness of the iceberg and its surroundings are comparable, or when one part of the iceberg is significantly lighter than other part. In this case, the image was rejected, which of course reduced the length of resulting time-series.

In general, 338 reliable and 45 partially reliable locations and spatial orientations of the iceberg D28 were derived from the C-band synthetic aperture radar measurements onboard Sentinel 1/A and Sentinel 1/B satellites for the period from 2019-09-25 to 2023-03-23 (1275 days).

2.2. Kinematic Characteristics

The iceberg linear velocity V was determined from loxodromic distances in the WGS84 reference coordinate system with the NAD83 datum. The iceberg area S was calculated as the number of cells with size of 1×1 km in the Lambert Conformal Conic map projection (LCC) coordinates. The iceberg mass M was calculated from the area S , taking into account the iceberg draft of 220–270 m, according to [Liu *et al.*, 2021], and the sea water density of $1,028 \text{ kg/m}^3$.

To calculate the azimuthal orientation α and angular rotation velocity ω , the shape of the iceberg was approximated by an ellipse, and the azimuthal angle α was defined as clockwise angle between the north direction and the semi-major axis position of the approximating ellipse. Axis direction ambiguity is 180° , therefore the iceberg was projected into the reference system associated with its center of mass and this axis was directed along the y ordinate. The direction with the largest number of matching pixels between a given iceberg shape and the reference shape was accepted as the true direction. Any iceberg image, for example, the first one, can be selected as a reference shape. Figure 1 represents various examples of projections associated with the center of mass and the direction of the iceberg semi-major axis, including initial AIS calving event. Reduction images to the unified projection promotes effective quality control in animation mode of identification results preview. To provide the maximal continuity of azimuthal orientation time-series, images with partially or not very reliable fixations were also taken into account.

The kinetic energy of the iceberg progressive motion was determined by the linear velocity V and the mass of the iceberg M :

$$K_v = \frac{MV^2}{2}.$$

The iceberg rotational energy was calculated from the angular velocity and moment of inertia:

$$K_\omega = \frac{J\omega^2}{2},$$

where ω – angular velocity $J = \sum_{i=1}^n m_i r_i^2$ – moment of inertia, m_i – mass of an ice column per i -cell, r_i – distance from the center of the i -cell to the center of iceberg mass (center of the approximating ellipse).

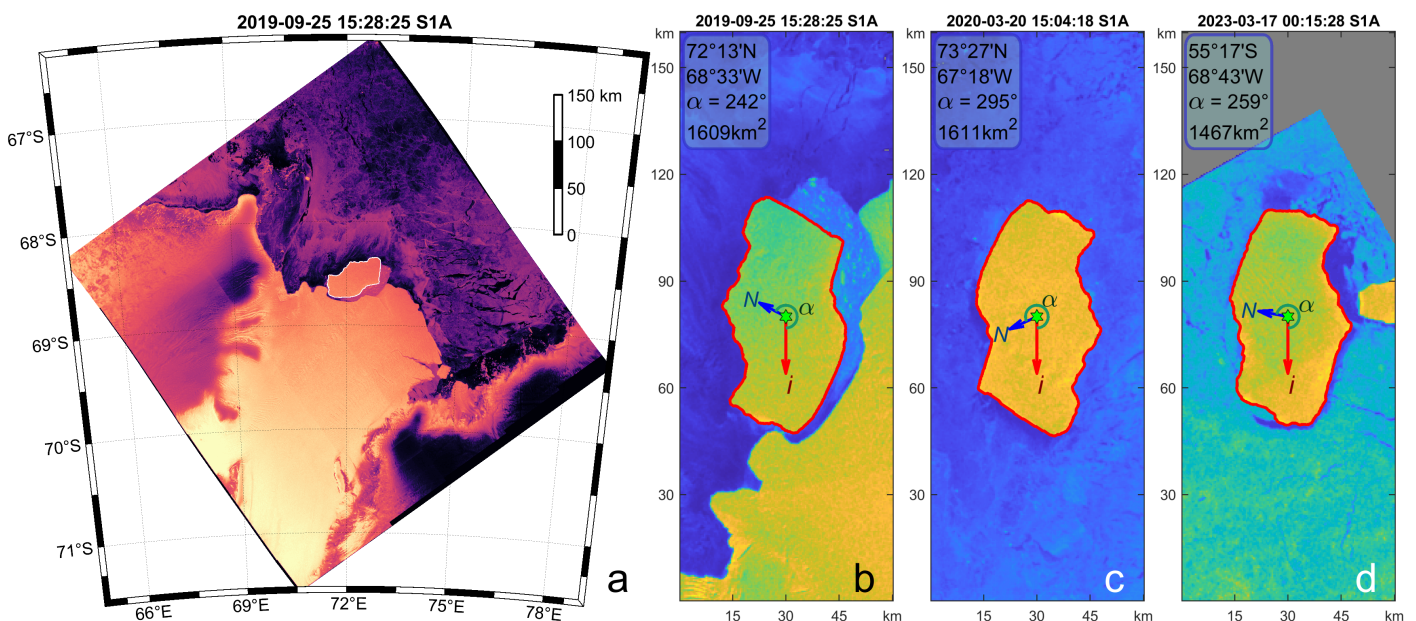


Figure 1. (a) Initial image of D28 calving from Amery Ice Shelf, iceberg boundaries are outlined by the white line; (b), (c) and (d) images in some time points of the iceberg D28 drift. N – direction to the North, i – orientation of the iceberg ellipse major semiaxis, α – azimuthal angle.

2.3. Iceberg Groundings

Determination of the iceberg grounding events was calculated as follows. The velocity $\mathbf{V} = \mathbf{i} \cdot V_x + \mathbf{j} \cdot V_y$ in a point $\mathbf{r} = \mathbf{i} \cdot x + \mathbf{j} \cdot y$ in a coordinate system moving at speed \mathbf{V}_0 is defined by the relation:

$$\mathbf{V} = \mathbf{V}_0 + \omega \times \mathbf{r},$$

where V_0 – forward velocity, $\omega = \mathbf{k} \times \omega$ – angular velocity of the coordinate system. The reference point in the coordinate system, for which at a given time $V_0 = 0$, is a stationary center of rotation. For it:

$$\mathbf{V} = \mathbf{i} \cdot V_x + \mathbf{j} \cdot V_y = \omega \times \mathbf{r} = \begin{vmatrix} \mathbf{i} & \mathbf{j} & \mathbf{k} \\ 0 & 0 & \omega \\ x & y & 0 \end{vmatrix} = -\mathbf{i} \cdot \omega \cdot y + \mathbf{j} \cdot \omega \cdot x,$$

which makes it possible to determine the coordinates of the stationary center of rotation. A possible indication of an iceberg grounding may be the matching this center with any point of the iceberg in several consecutive images.

3. Results and Discussion

3.1. Drift Trajectory

The drift trajectories of icebergs D28 as well as other recent gigantic icebergs A68 and A76 (Figure 2) correspond to the general pattern of a steady, nearly continuous ice transport around Antarctic: eastward in the Antarctic Circumpolar Current (ACC) and westward along the continental coast [Emery *et al.*, 1997].

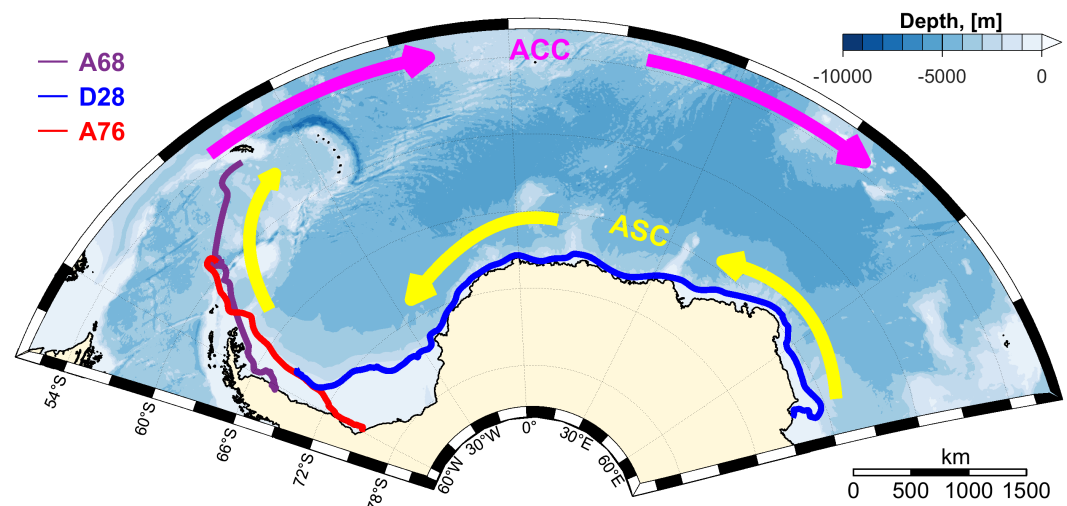


Figure 2. Trajectories of icebergs A68, D28 and A76. Labelling: ACC – Antarctic Circumpolar Current, ASC – Antarctic Slope Current.

The motion of icebergs along the continental coast is exerted by various forcing: easterly katabatic winds, the Antarctic Coastal Current and, for the most part, the Antarctic Slope Front/Antarctic Slope Current (ASC) system [Jacobs, 1991]. Due to a weak density stratification the geographical position of ASC is largely determined by the bottom topography (conservation of potential vorticity f/H) and mainly corresponds to the isobath of 1,000 m or 400–500 m in certain areas of the continental slope [Azaneu *et al.*, 2017; Gill, 1973; Heywood *et al.*, 2004; Whitworth *et al.*, 2013].

Iceberg D28 traveled more than 6,000 km along the Antarctic coast over 1,275 days for the period under review (from 2019-09-25 to 2023-03-23) (Figure 3). Changes in its characteristics (size, mass, speed, etc.) have a well-defined regional nature: 1st section of the iceberg drift is the leg from Prydz Bay in the Commonwealth Sea to the Cosmonauts Sea (0–550 days), 2nd section is the path from the Riiser-Larsen Sea to the Brunt Ice Shelf in the northeastern part of the Weddell Sea (550–800 days) and 3rd section is wide shelf part of the Weddell Sea (> 800 days of the drift).

3.2. Kinematic Characteristics

Variations of the iceberg area in the 1st drift section ranged from 1,560 to 1,630 km², decreasing on average from 1,600 to 1,570 km² (Figure 4). Small changes of the estimated

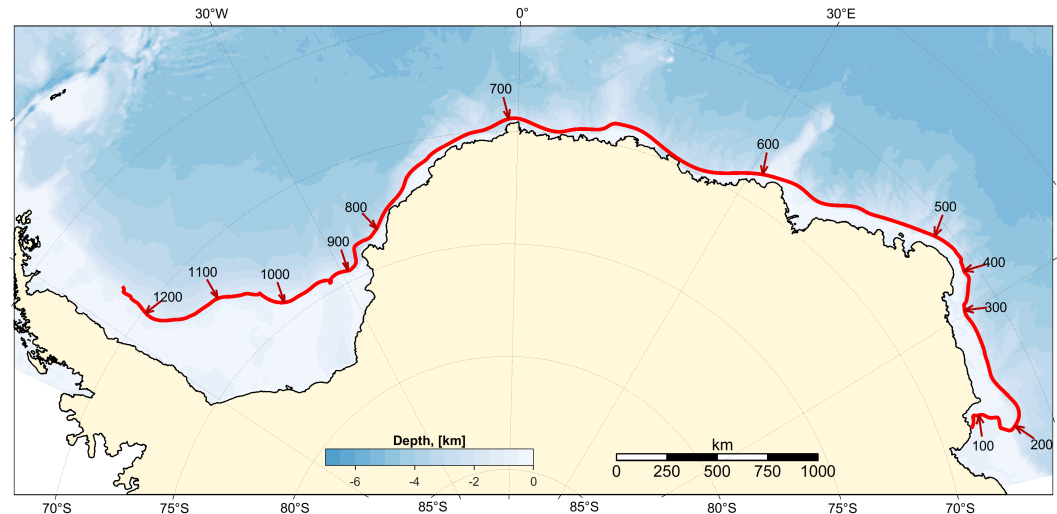


Figure 3. The iceberg D28 path along the Antarctic coast, digits denote the drift duration in days.

iceberg geometric dimensions are caused not only by methodical errors of determining its boundaries, but also with the physical processes of addition/loss of smaller floating ice cover. After crossing the underwater Gunnerus Ridge between the Cosmonauts Sea and the Riiser-Larsen Sea, iceberg D28 began rapidly reduce its size and mass, especially in the Riiser-Larsen Sea and the Lazarev Sea. The iceberg area during the 2nd drift section decreased on average from 1,570 to 1,460 km². After entering the open part of the Weddell Sea, the size of D28 was stabilized, with a slight increase in the western part of the sea (> 1,200 days of the drift).

During the drift period of consideration (3.5 years), iceberg D28 made 13 complete anticyclonic rotations (counterclockwise in the southern hemisphere), of which 9 cycles occurred in the second year of drift while passing from the Cosmonauts Sea to the eastern part of the Weddell Sea (Figure 4).

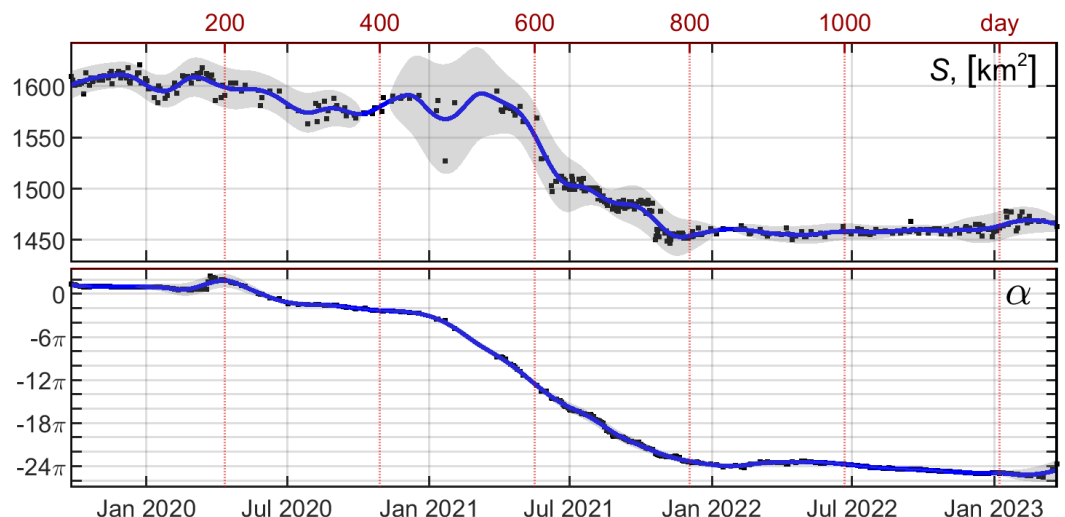


Figure 4. Time-series of area S and azimuth orientation α of the iceberg D28. The 95%-confidence level is painted over by grey color.

The linear velocity of iceberg D28 (Figure 5) was maximal in the 2nd section of the drift (from 30°W to 20°E), reaching 20–30 cm/s in the vicinity of the underwater Gunnerus Ridge and the Fimbul Ice Shelf (0–5°E). The iceberg moving speed within 1st and 3rd sections generally in 5–10 times lower than speed in the 2nd section, except some local maxima in the Commonwealth Sea (65°–70°E) and the Weddell Sea (35°–40°W), reaching 5–10 cm/s. Regional features of the angular speed are similar to those of the linear velocity

(Figure 5). The iceberg rotates much more intensely in the 2nd drift section, and the local maximum of linear velocity in the Commonwealth Sea tightly corresponds to the increase in angular speed, while the local velocity maximum in the Weddell Sea has less influence on the angular velocity. When D28 rounded the Brunt Ice Shelf (25°W), an increase of angular velocity with reverse (cyclonic) rotation was observed.

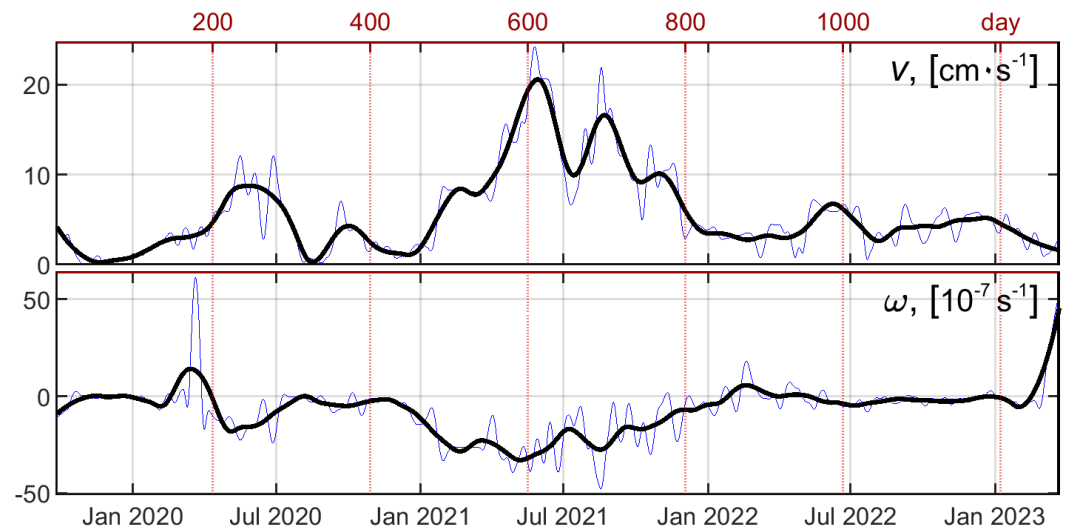


Figure 5. Time-series of linear V and angular ω velocity of the iceberg D28. Bold line represents data smoothed by regression 1st degree polynomial filter (120-day window).

Since the mass and moment of inertia were calculated via the surface area of the iceberg, these characteristics vary in accordance with iceberg dimensions, that is, they sharply decrease in the 2nd section of the trajectory and stabilize when reaching a wide shelf of the Weddell Sea (Figure 6). Distribution of the iceberg kinetic energy qualitatively corresponds to variations of linear and angular velocities, taking into account the mass loss of D28 during the drift (Figure 7).

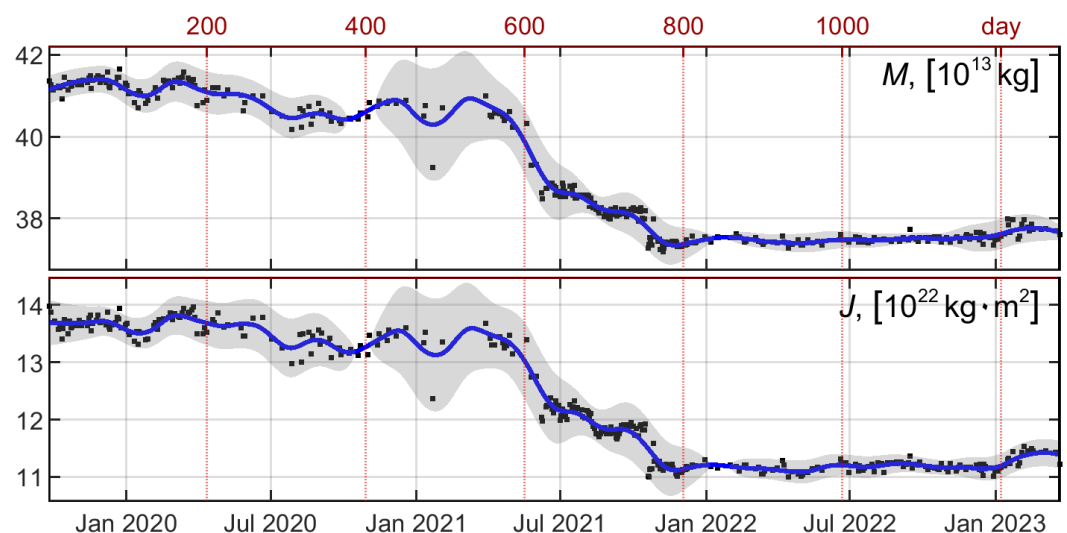


Figure 6. Time-series of mass M and moment of inertia J of the iceberg D28. The 95%-confidence level is painted over by grey color.

Noteworthy is the high consistency of the iceberg D28 time-series V and ω . For example, icebergs A68 and A76, started in other oceanographic conditions (in the region of the Antarctic Peninsula), do not manifest such a high correlation between V and ω .

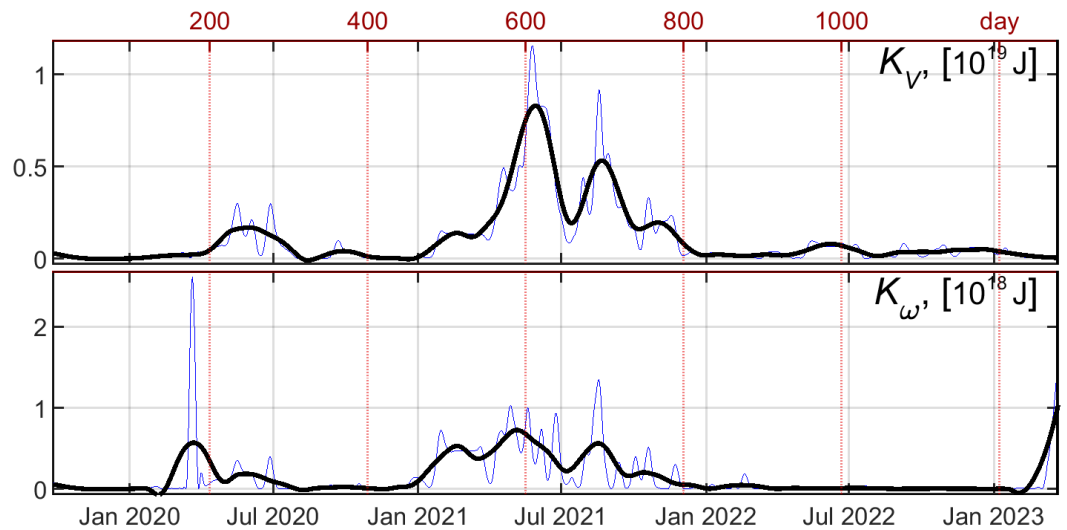


Figure 7. Time-series of kinetic K_V and rotational K_ω energy of the iceberg D28.

Obviously, in a case of coastal current, flow vorticity will primarily depend on shear instability, which is determined by the lateral velocity gradient, i.e. by current speed and distance from the shore. To assess a contribution of this simple mechanism to the general vorticity of the iceberg’s motion, a linear regression model was used:

$$\omega = A + B \cdot \Omega,$$

where ω – observed angular velocity, $\Omega = V/D/2$ – model angular velocity, V – linear velocity, D – nearest distance from the iceberg to the shore, $A = -3.2033 \times 10^{-7}$, $B = 1.1649$.

Figure 8 shows the distance D and superposition of angular velocities ω and Ω . Despite the rough assumptions (the inertia of the iceberg is not taken into account, the gradient assumed as linear, the distance is measured to a zero depth value when the iceberg draft is about 250 m, other vorticity components are not examined), the correlation between ω and Ω is distinctly high ($R = 0.76$, $R^2 = 0.57$, with a vanishingly small probability of the null hypothesis). Thus, about 57% of the variability of the iceberg angular velocity ω can be explained by the simple mechanism of linear flow shear near the coastline.

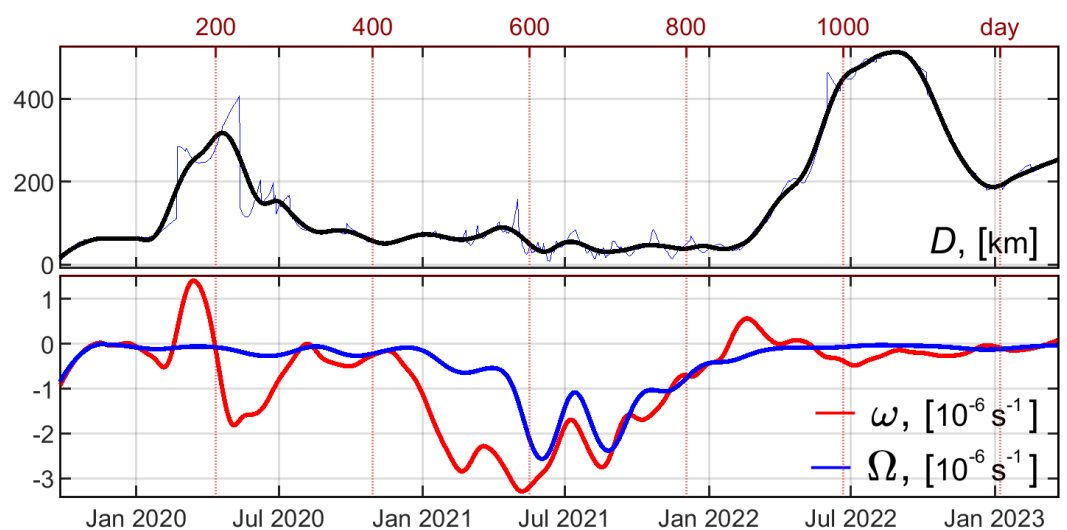


Figure 8. Distance D between the shore and the iceberg D28, angular velocities: observed ω and model Ω .

3.3. Iceberg Groundings

The underwater draft (220–270 m) and groundings of iceberg D28 at the initial stage of its drift in August–September 2020 were revealed in [Liu *et al.*, 2021], using altimeter data from the Cryosat-2, Sentinel-3, and ICESat 2 satellites. According to the digital bottom relief gridded products Bedmap2 and BedMachine, the depths at these points are greater than the iceberg draft by 570 m and 350 m, respectively. This once again is an evidence of the rugged bottom topography in the coastal zone of Antarctic and the insufficient number of hydrographic surveys. Spatial localization of iceberg groundings can be useful for correcting and clarifying the underwater topography of these areas.

According to the above described method for calculating locations of motionless rotation centers, 23 cases of probable iceberg D28 groundings were identified. Examples of the iceberg rotation and motion during these events are presented in Figure 9. Grounding point locations and their depth according to ETOPO_2022_v1_15s gridded data are given in Table 1. Some of these points are very close in time and space, so they probably represent the same grounding events. Negative values of angular velocity ω relative to a stationary center of rotation correspond to anticyclonic movement. In several cases, the iceberg changed the prevailing anticyclonic rotation to the cyclonic one (Figure 9c).

During the iceberg braking episodes, huge angular rotation velocities have been revealed (Table 1). These events are not associated with a weakening of background currents and visual analysis of corresponding images does not confirm ice-bound conditions or pressing iceberg against the ice edge. All detected stationary centers of rotation are located inside the iceberg and are most likely the places where D28 took aground.

Table 1. Grounding events and rotation velocity of the iceberg D28 around stationary points

| From date | To date | Longitude | Latitude | $\omega, 10^{-4}$ cycle/day | H, m |
|------------|------------|-----------|-----------|--------------------------------|--------|
| 2019-10-24 | 2019-10-26 | 70°47.5'E | 68°29.5'S | −17 | 800 |
| 2019-11-05 | 2019-11-07 | 70°53.6'E | 68°20.7'S | −25 | 730 |
| 2019-11-17 | 2019-11-19 | 70°42.8'E | 68°12.2'S | −35 | 395 |
| 2020-01-16 | 2020-01-18 | 70°54.8'E | 67°58.3'S | −28 | 499 |
| 2020-01-28 | 2020-02-04 | 71°1.6'E | 67°33.7'S | −72 | 409 |
| 2020-03-18 | 2020-03-20 | 73°13.1'E | 67°16.4'S | −112 | 539 |
| 2020-03-20 | 2020-03-23 | 73°11.3'E | 67°14.5'S | −312 | 541 |
| 2020-08-10 | 2020-08-18 | 58°27.3'E | 66°25.2'S | −54 | 545 |
| 2020-08-18 | 2020-08-20 | 58°59.4'E | 66°17.1'S | −33 | 1,870 |
| 2020-08-30 | 2020-09-01 | 59°25.7'E | 66°25.1'S | −12 | 2,154 |
| 2020-09-03 | 2020-09-11 | 58°26.0'E | 66°23.0'S | −93 | 479 |
| 2020-09-11 | 2020-09-13 | 58°33.4'E | 66°18.5'S | −117 | 478 |
| 2020-10-19 | 2020-10-21 | 56°22.1'E | 65°46.4'S | −184 | 507 |
| 2020-11-24 | 2020-11-26 | 54°37.2'E | 65°31.6'S | 17 | 774 |
| 2021-11-25 | 2021-11-30 | 21°5.3'W | 73°23.1'S | −164 | 284 |
| 2022-02-17 | 2022-02-19 | 27°44.7'W | 74°18.7'S | 356 | 2,319 |
| 2022-03-07 | 2022-03-11 | 27°49.0'W | 74°33.0'S | 16 | 1,726 |
| 2022-07-20 | 2022-07-24 | 42°42.0'W | 73°13.4'S | −176 | 1,408 |
| 2022-07-24 | 2022-07-29 | 42°37.0'W | 73°22.4'S | −83 | 1,263 |
| 2022-08-29 | 2022-09-01 | 45°48.6'W | 72°42.6'S | −82 | 1,182 |
| 2022-11-12 | 2022-11-13 | 52°25.6'W | 71°33.4'S | 149 | 1,775 |
| 2023-01-04 | 2023-01-05 | 55°44.9'W | 70°5.8'S | 75 | 1,176 |
| 2023-02-27 | 2023-03-05 | 55°38.6'W | 68°41.3'S | −105 | 1,238 |

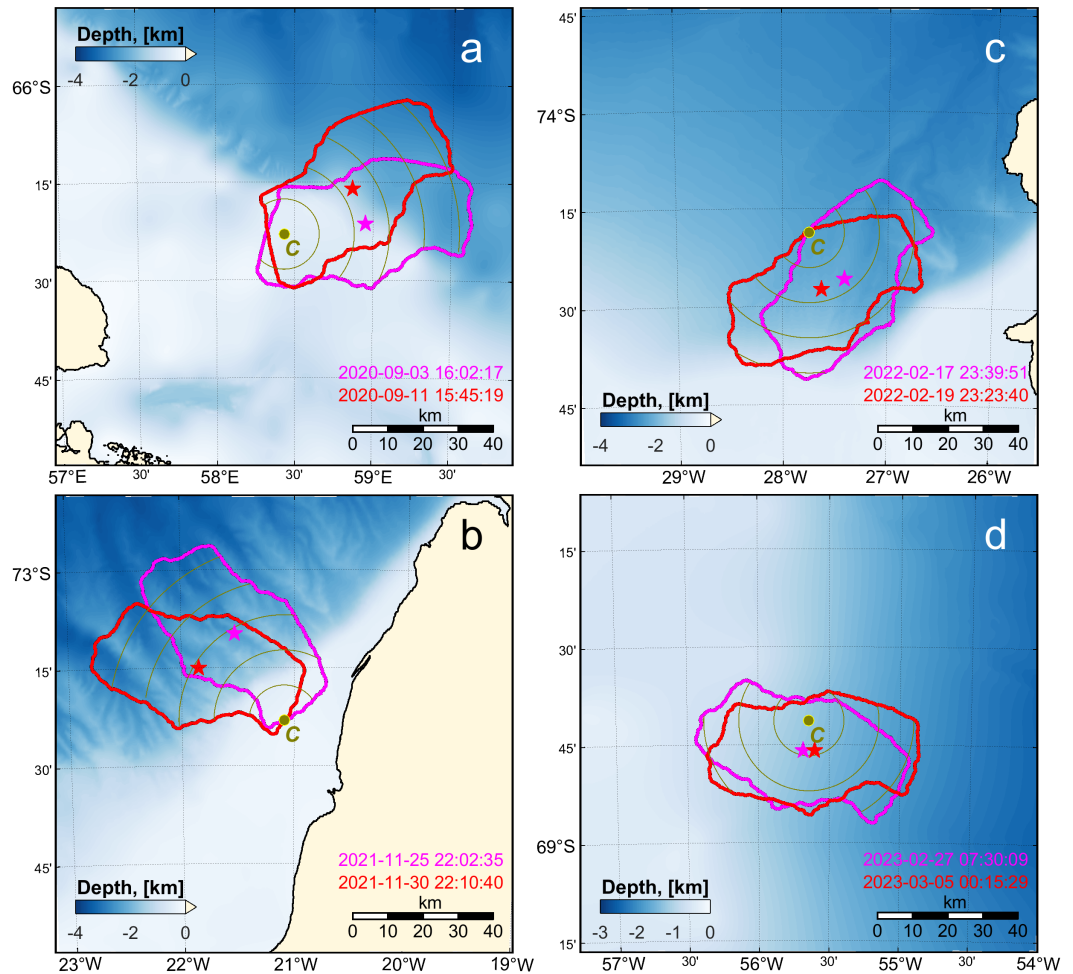


Figure 9. Iceberg D28 positions during grounding events. (a) Region of the Kemp Land in the Commonwealth Sea in September 2020, (b), (c) region of the Brunt ice shelf in the Weddell Sea in November 2021, February 2022, (d) region of the Larsen ice shelf in the Weddell Sea, March 2023. Green circles show centers of rotation, asterisks denote centers of the iceberg mass.

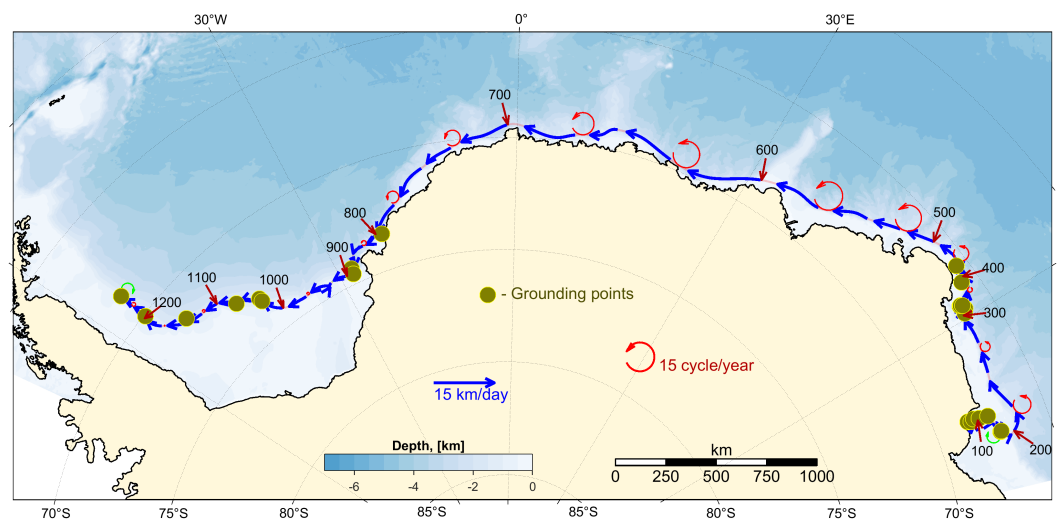


Figure 10. Locations of possible groundings of the iceberg D28. Drift vectors present 20-day movements with 5-day intervals between them. “Circle vectors”, presented angular velocities ω , are drawn with 50-day intervals. Vector linear dimensions are proportional values of V and ω and the legend.

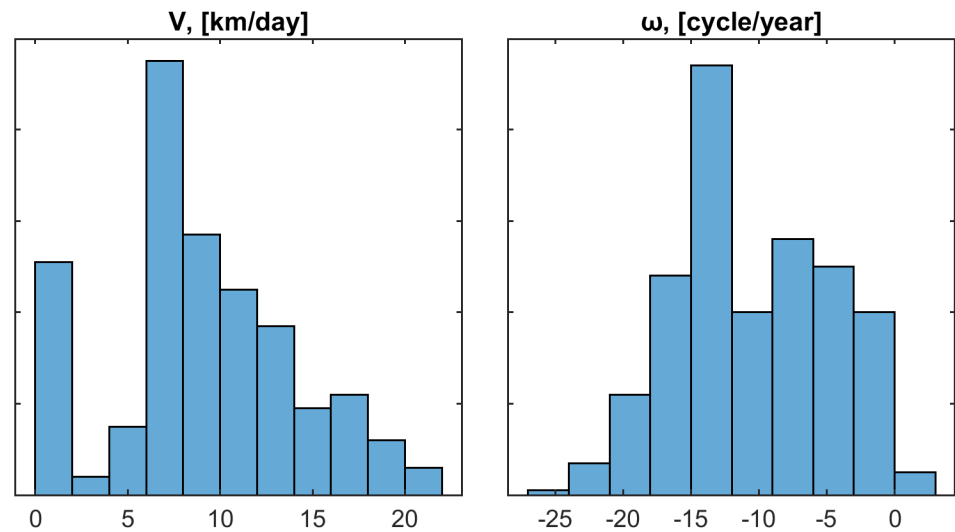


Figure 11. Histograms of linear velocity V and angular velocity ω in the non-stop section of the iceberg D28 drift.

Locations of possible iceberg D28 groundings, drift vectors and the “circular vectors” of the rotation angular velocity are shown in Figure 10. During the drift period from 26-11-2020 to 25-11-2021 along the Bellingshausen Ice Shelf from the Kemp Land ($54^{\circ}37.2'E$, $65^{\circ}31.6'S$) to the Cape Vestkapp ($21^{\circ}31.6'W$, $73^{\circ}9.8'S$) no cases of touching the bottom were found. It can be considered that in this section of the drift, the kinematic characteristics of the D28 motion are the most representative for integral flux in the layer of the iceberg draft (about 250 m). Figure 11 and Table 2 present statistics of linear velocity V and angular velocity ω in this non-stop section of the iceberg D28 trajectory.

Table 2. Statistics of linear velocity V and angular velocity ω in the non-stop section of the iceberg D28 drift

| | V , km/day | ω , cycle/year |
|--------------------|--------------|-----------------------|
| Maximum | 20.9 | -24.1 |
| Median | 8.81 | -11.6 |
| Average | 9.2 | -10.5 |
| Standard deviation | 4.9 | 5.6 |

4. Conclusions

The ongoing variations of the iceberg kinematic characteristics during D28 drift along the Antarctic coast are in fairly good agreement with the classification of the frontal and dynamic structure of the Antarctic Slope Current presented in [Thompson *et al.*, 2018]. The 2nd section of the D28 trajectory (from the Riiser-Larsen Sea to the Brunt Ice Shelf), with the highest speed of motion and rotation, falls on the “fresh shelf” category (according to the classification [Thompson *et al.*, 2018]). Here the ASC velocity is maximal, due to the strong katabatic easterly winds and a sharp slope thermohaline front, extending from the sea surface to the bottom. High velocity and fast rotation in this area most likely lead to intensification of mechanical destruction and a rapid decrease of the iceberg size and mass. The 1st and 3rd sections of the D28 trajectory (Commonwealth Sea, Cosmonauts Sea and Weddell Sea) according to the classification [Thompson *et al.*, 2018] belong to the “dense shelf”. Easterly winds in these regions weaken, dense shelf waters, descending down the continental slope, displace the thermohaline front to the sea surface and the ASC speed decreases. The motion of iceberg D28 is significantly slowing down, the area and mass of the iceberg become stabilized.

Localization of the iceberg D28 grounding sites within the 1st and 3rd sections of the drift can be associated with several factors: weakening of the ASC, which favoured to the iceberg deceleration even while soft bottom contact occurs, complicated underwater terrain in the form of ridges and canyons, strong eddy structures, which disturbing the iceberg path with deviations towards shallower depths. According to studies of ASC mesoscale and submesoscale variability [Azaneu *et al.*, 2017; Stewart and Thompson, 2015; Wang *et al.*, 2009], emergence and development of eddies is often associated with jets of dense shelf water descending along the continental slope to participate further in the Antarctic Bottom Water (AABW) formation. Such processes are intrinsic to “dense shelves” (according to the classification [Thompson *et al.*, 2018]), which include the 1st and 3rd sections of the D28 drift. Low ASC speed also reduces stream stability and increases meandering, bending iceberg paths.

The contribution of linear shear instability to ASC vorticity is significantly reduced in the Commonwealth Sea, where the southern boundary of the ACC zone approaches the counter-directed ASC, as well in the Kemp Land and Brunt Ice Shelf regions.

In general, drifting icebergs, in addition to their practical, ecological and climatic significance, can be considered in a certain sense as a tool that allows to assess indirectly some oceanographic processes in Antarctic.

Acknowledgments. This research was funded by Marine Hydrophysical Institute RAS, State Tasks FNNN-2021-0010, FNNN-2024-0014.

References

- Azaneu, M., K. J. Heywood, B. Y. Queste, and A. F. Thompson (2017), Variability of the Antarctic Slope Current System in the Northwestern Weddell Sea, *Journal of Physical Oceanography*, 47(12), 2977–2997, <https://doi.org/10.1175/JPO-D-17-0030.1>.
- Barbat, M. M., T. Rackow, C. Wesche, et al. (2021), Automated iceberg tracking with a machine learning approach applied to SAR imagery: A Weddell sea case study, *ISPRS Journal of Photogrammetry and Remote Sensing*, 172, 189–206, <https://doi.org/10.1016/j.isprsjprs.2020.12.006>.
- Barnes, D. K. A., and T. Souster (2011), Reduced survival of Antarctic benthos linked to climate-induced iceberg scouring, *Nature Climate Change*, 1(7), 365–368, <https://doi.org/10.1038/nclimate1232>.
- Budge, J. S., and D. G. Long (2018), A Comprehensive Database for Antarctic Iceberg Tracking Using Scatterometer Data, *IEEE Journal of Selected Topics in Applied Earth Observations and Remote Sensing*, 11(2), 434–442, <https://doi.org/10.1109/JSTARS.2017.2784186>.
- Canny, J. (1986), A Computational Approach to Edge Detection, *IEEE Transactions on Pattern Analysis and Machine Intelligence*, PAMI-8(6), 679–698, <https://doi.org/10.1109/TPAMI.1986.4767851>.
- Emery, W. J., C. W. Fowler, and J. A. Maslanik (1997), Satellite-derived maps of Arctic and Antarctic sea ice motion: 1988 to 1994, *Geophysical Research Letters*, 24(8), 897–900, <https://doi.org/10.1029/97GL00755>.
- Francis, D., K. S. Mattingly, S. Lhermitte, M. Temimi, and P. Heil (2021), Atmospheric extremes triggered the biggest calving event in more than 50 years at the Amery Ice shelf in September 2019, *The Cryosphere*, 15, 2147–2165, <https://doi.org/10.5194/tc-2020-219>.
- Fricker, H. A., N. W. Young, I. Allison, and R. Coleman (2002), Iceberg calving from the Amery Ice Shelf, East Antarctica, *Annals of Glaciology*, 34, 241–246, <https://doi.org/10.3189/172756402781817581>.
- Gandhi, P. P., and S. A. Kassam (1988), Analysis of CFAR processors in nonhomogeneous background, *IEEE Transactions on Aerospace and Electronic Systems*, 24(4), 427–445, <https://doi.org/10.1109/7.7185>.
- Gill, A. E. (1973), Circulation and bottom water production in the Weddell Sea, *Deep Sea Research and Oceanographic Abstracts*, 20(2), 111–140, [https://doi.org/10.1016/0011-7471\(73\)90048-X](https://doi.org/10.1016/0011-7471(73)90048-X).
- Greenbaum, J. S., D. D. Blankenship, D. A. Young, et al. (2015), Ocean access to a cavity beneath Totten Glacier in East Antarctica, *Nature Geoscience*, 8(4), 294–298, <https://doi.org/10.1038/ngeo2388>.

- Heywood, K. J., A. C. Naveira Garabato, D. P. Stevens, and R. D. Muench (2004), On the fate of the Antarctic Slope Front and the origin of the Weddell Front, *Journal of Geophysical Research: Oceans*, 109(C6), <https://doi.org/10.1029/2003JC002053>.
- Hogg, A. E., and G. H. Gudmundsson (2017), Impacts of the Larsen-C Ice Shelf calving event, *Nature Climate Change*, 7(8), 540–542, <https://doi.org/10.1038/nclimate3359>.
- Jacobs, S. S. (1991), On the nature and significance of the Antarctic Slope Front, *Marine Chemistry*, 35(1–4), 9–24, [https://doi.org/10.1016/S0304-4203\(09\)90005-6](https://doi.org/10.1016/S0304-4203(09)90005-6).
- King, M. A., R. Coleman, A.-J. Freemantle, et al. (2009), A 4-decade record of elevation change of the Amery Ice Shelf, East Antarctica, *Journal of Geophysical Research: Earth Surface*, 114(F1), <https://doi.org/10.1029/2008JF001094>.
- Li, T., Y. Liu, and X. Cheng (2020), Recent and imminent calving events do little to impair Amery ice shelf's stability, *Acta Oceanologica Sinica*, 39(5), 168–170, <https://doi.org/10.1007/s13131-020-1600-6>.
- Liu, X., X. Cheng, Q. Liang, et al. (2021), Grounding Event of Iceberg D28 and Its Interactions with Seabed Topography, *Remote Sensing*, 14(1), 154, <https://doi.org/10.3390/rs14010154>.
- Liu, Y., J. C. Moore, X. Cheng, et al. (2015), Ocean-driven thinning enhances iceberg calving and retreat of Antarctic ice shelves, *Proceedings of the National Academy of Sciences*, 112(11), 3263–3268, <https://doi.org/10.1073/pnas.1415137112>.
- Matas, J., O. Chum, M. Urban, and T. Pajdla (2004), Robust wide-baseline stereo from maximally stable extremal regions, *Image and Vision Computing*, 22(10), 761–767, <https://doi.org/10.1016/j.imavis.2004.02.006>.
- Mazur, A. K., A. K. Wåhlin, and A. Krężel (2017), An object-based SAR image iceberg detection algorithm applied to the Amundsen Sea, *Remote Sensing of Environment*, 189, 67–83, <https://doi.org/10.1016/j.rse.2016.11.013>.
- McIlhagga, W. (2010), The Canny Edge Detector Revisited, *International Journal of Computer Vision*, 91(3), 251–261, <https://doi.org/10.1007/s11263-010-0392-0>.
- Mitkari, K., J. Pallipad, D. Putrevu, and A. Misra (2021), Detecting Calving Events of Icebergs D-28 and B-49 using High Resolution Sentinel-1A SAR Data, *EGU General Assembly 2021, online, 19-30 Apr 2021, EGU21-16264*, <https://doi.org/10.5194/egusphere-egu21-16264>.
- Morozov, E. G., V. A. Krechik, D. I. Frey, and V. V. Zamshin (2021), Currents in the Western Part of the Weddell Sea and Drift of Large Iceberg A68A, *Oceanology*, 61(5), 589–601, <https://doi.org/10.1134/S000143702105009X>.
- Normandeau, A., K. MacKillop, M. Macquarrie, et al. (2021), Submarine landslides triggered by iceberg collision with the seafloor, *Nature Geoscience*, 14(8), 599–605, <https://doi.org/10.1038/s41561-021-00767-4>.
- Otsu, N. (1979), A Threshold Selection Method from Gray-Level Histograms, *IEEE Transactions on Systems, Man, and Cybernetics*, 9(1), 62–66, <https://doi.org/10.1109/TSMC.1979.4310076>.
- Pogrebnoi, A. E. (2023), Estimation of Internal Wave Parameters in the Arctic Based on Synthetic Aperture Satellite Radar Data, *Physical Oceanography*, 30(1), 98–111, <https://doi.org/10.29039/1573-160X-2023-1-98-111>.
- Pritchard, H. D., S. R. M. Ligtenberg, H. A. Fricker, et al. (2012), Antarctic ice-sheet loss driven by basal melting of ice shelves, *Nature*, 484(7395), 502–505, <https://doi.org/10.1038/nature10968>.
- Shepherd, A., H. A. Fricker, and S. L. Farrell (2018), Trends and connections across the Antarctic cryosphere, *Nature*, 558(7709), 223–232, <https://doi.org/10.1038/s41586-018-0171-6>.
- Silva, T. A. M., and G. R. Bigg (2005), Computer-based identification and tracking of Antarctic icebergs in SAR images, *Remote Sensing of Environment*, 94(3), 287–297, <https://doi.org/10.1016/j.rse.2004.10.002>.
- Singh, K. N., R. K. Singh, M. Maisnam, et al. (2021), Detection of Two Recent Calving Events in Antarctica from SCATSAT-1, in *2021 IEEE International Geoscience and Remote Sensing Symposium IGARSS*, pp. 439–442, IEEE, <https://doi.org/10.1109/IGARSS47720.2021.9553306>.
- Singh, K. N., M. Maisnam, R. K. Singh, et al. (2023), Spatio-temporal monitoring of the iceberg D28 using SCATSAT-1 data, *Polar Record*, 59, <https://doi.org/10.1017/S0032247423000062>.

- Smith, J. A., A. G. C. Graham, A. L. Post, et al. (2019), The marine geological imprint of Antarctic ice shelves, *Nature Communications*, 10(1), <https://doi.org/10.1038/s41467-019-13496-5>.
- Stewart, A. L., and A. F. Thompson (2015), Eddy-mediated transport of warm Circumpolar Deep Water across the Antarctic Shelf Break, *Geophysical Research Letters*, 42(2), 432–440, <https://doi.org/10.1002/2014GL062281>.
- Stuart, K. M., and D. G. Long (2011), Tracking large tabular icebergs using the SeaWinds Ku-band microwave scatterometer, *Deep Sea Research Part II: Topical Studies in Oceanography*, 58(11–12), 1285–1300, <https://doi.org/10.1016/j.dsr2.2010.11.004>.
- Thompson, A. F., A. L. Stewart, P. Spence, and K. J. Heywood (2018), The Antarctic Slope Current in a Changing Climate, *Reviews of Geophysics*, 56(4), 741–770, <https://doi.org/10.1029/2018RG000624>.
- Walker, C. C., M. K. Becker, and H. A. Fricker (2021), A High Resolution, Three-Dimensional View of the D-28 Calving Event From Amery Ice Shelf With ICESat-2 and Satellite Imagery, *Geophysical Research Letters*, 48(3), <https://doi.org/10.1029/2020GL091200>.
- Wang, Q., S. Danilov, and J. Schröter (2009), Bottom water formation in the southern Weddell Sea and the influence of submarine ridges: Idealized numerical simulations, *Ocean Modelling*, 28(1–3), 50–59, <https://doi.org/10.1016/j.ocemod.2008.08.003>.
- Whitworth, T., A. H. Orsi, S.-J. Kim, W. D. Nowlin, and R. A. Locarnini (2013), *Water Masses and Mixing Near the Antarctic Slope Front*, pp. 1–27, American Geophysical Union, <https://doi.org/10.1029/AR075p0001>.
- Yu, Y., Z. Zhang, M. Shokr, et al. (2019), Automatically Extracted Antarctic Coastline Using Remotely-Sensed Data: An Update, *Remote Sensing*, 11(16), 1844, <https://doi.org/10.3390/rs11161844>.
- Zhu, T., X. Cui, and Y. Zhang (2021), Analysis of Temporal and Spatial Variability of Fronts on the Amery Ice Shelf Automatically Detected Using Sentinel-1 SAR Data, *Remote Sensing*, 13(17), 3528, <https://doi.org/10.3390/rs13173528>.